International Journal of Engineering & Extended Technologies Research (IJEETR)

|ISSN: 2322-0163| www.ijeetr.com | A Bimonthly, Peer Reviewed, Scholarly Indexed Journal |

| Volume 8, Issue 3, May - June 2026 |

DOI:10.15662/IJEETR.2026.0803008

NeuroSeg Decoding the Brain a Multimodal Intelligence Framework for MRI Brain Tissue Segmentation Methods Machines and Medicine

S. SathishKumar[1], V. Ellappan[2], M Bharanidharan [3], M. SathishKumar [4], R.Sivakumar [5]

Associate Professor, Department of ECE, Mahendra Institute of Technology, Namakkal, Tamil Nadu, India[1]

Professor, Department of ECE, Mahendra Institute of Technology, Namakkal, Tamil Nadu, India[2]

Assistant Professor, Department of ECE, Mahendra Institute of Technology, Namakkal, Tamil Nadu, India[3,4]

Assistant Professor, Paavai Engineering College (Autonomous), Namakkal, Tamil Nadu, India[5]

Publication History: Received: 25.04.2026; Revised: 01.05.2026; Accepted: 03.05. 2026; Published: 09.05.2026.

ABSTRACT: Magnetic Resonance Imaging (MRI) brain segmentation is a cornerstone of neuroimaging analysis, enabling clinicians and researchers to precisely delineate white matter (WM), gray matter (GM), and cerebrospinal fluid (CSF) compartments. This comprehensive review spans classical intensity-based methods (thresholding, k-means, fuzzy C-means), probabilistic atlas-guided frameworks (Expectation-Maximization, Gaussian Mixture Models), deformable surface models (active contours, level sets), and contemporary deep learning architectures including 3D U-Net, nnU-Net, and Swin-UNet transformers. Essential preprocessing stages — bias field correction (N4ITK), skull stripping (BET, HD-BET), and multimodal image registration (ANTs SyN) — are examined with original synthesised MRI visualisations illustrating each stage. The partial volume effect (PVE) and its correction strategies are discussed in detail. Validation methodologies using BrainWeb phantoms and the IBSR real-data repository are described alongside Dice similarity and Jaccard index benchmarks. Emerging frontiers including federated learning for privacy-preserving multi-site studies, uncertainty quantification, self-supervised pretraining, and neuroimaging foundation models are critically reviewed. This article serves as a structured reference for clinical researchers, biomedical engineers, and AI practitioners engaged in brain MRI analysis.

KEYWORDS: MRI brain segmentation · white matter · gray matter · deep learning · U-Net · nnU-Net · transformer · fuzzy C-means · atlas-based methods · bias field correction · partial volume effect · Dice coefficient · federated learning · neuroimaging

I. INTRODUCTION

Magnetic Resonance Imaging (MRI) stands as the premier non-invasive modality for structural brain analysis in living subjects. Unlike computed tomography (CT), which exposes patients to ionising radiation, or positron emission tomography (PET), which requires radioactive tracers, MRI exploits the differential relaxation times of hydrogen nuclei across tissue types to generate high-contrast volumetric images with no known biological hazard at standard clinical field strengths [1]. This combination of safety, spatial resolution (typically 1 mm isotropic at 1.5T–3T), and rich tissue contrast has made MRI the workhorse of neurological diagnosis, surgical planning, and neuroscientific research.

Brain MRI segmentation — the computational process of partitioning the acquired volume into anatomically or functionally coherent regions — underpins virtually every quantitative neuroimaging workflow. Clinical applications include volumetric assessment of cortical atrophy in Alzheimer's disease, delineation of tumor margins for neurosurgical and radiotherapy planning, mapping of lesion burden in multiple sclerosis, evaluation of cortical dysplasia in epilepsy, and developmental trajectory analysis in neonatal and pediatric cohorts [2,3]. The accuracy of downstream measurements — gray matter volume, cortical thickness, white matter tract integrity — is directly governed by the quality of the initial segmentation.

Manual segmentation by expert neuroradiologists demands that trained operators trace anatomical boundaries across 80–120 coronal slices per volume, requiring 4–8 hours per scan. This effort is not only prohibitively expensive for large cohort studies but is also subject to substantial intra- and inter-rater variability, with Dice coefficients between expert

International Journal of Engineering & Extended Technologies Research (IJEETR)

|ISSN: 2322-0163| www.ijeetr.com | A Bimonthly, Peer Reviewed, Scholarly Indexed Journal |

| Volume 8, Issue 3, May - June 2026 |

DOI:10.15662/IJEETR.2026.0803008

annotators rarely exceeding 0.85 for cortical structures [4]. Automated and semi-automated methods therefore occupy a critical role in translating MRI data into reproducible quantitative biomarkers.

The evolution of automated brain MRI segmentation spans three broad technological generations. Classical intensity-based methods (1980s–2000s) exploited the trimodal intensity histogram of bias-corrected brain MRI to classify voxels into WM, GM, and CSF using thresholding, region growing, and iterative clustering algorithms. Probabilistic model-based methods (1990s–2010s) introduced Bayesian inference, Gaussian Mixture Models (GMMs), Markov Random Field (MRF) spatial regularisation, and probabilistic brain atlases. The current deep learning era (2015–present) harnesses convolutional neural networks and, most recently, vision transformers achieving Dice scores exceeding 0.93 for primary tissue classes [5].

II. FUNDAMENTAL CONCEPTS IN MRI BRAIN SEGMENTATION

2.1 Image Representation: Pixels, Voxels, and Intensity

A two-dimensional MRI slice is formalised as a function I(i,j) defined over a spatial lattice of M×N pixels, where each pixel carries an integer intensity value in [0,255] reflecting the average magnetic resonance characteristics of the underlying tissue element. Extending to three-dimensional volumetric acquisition, the representation becomes I(i,j,k) over M×N×D voxels [1]. Standard clinical neuroimaging encodes intensity in 12–16 bits (4096–65536 grey levels), typically downsampled to 8 bits for processing. Voxel dimensions in contemporary brain MRI protocols range from 1×1×1 mm isotropic in standard 3T T1-weighted (T1-W) MPRAGE sequences to 0.5 mm isotropic in research-grade 7T acquisitions.

2.2 Brain Tissue Classes and Intensity Distributions

Structural brain MRI segmentation classically targets three primary compartments: White Matter (WM), Gray Matter (GM), and Cerebrospinal Fluid (CSF). In bias-corrected T1-weighted MRI of a healthy adult brain, WM appears brightest (high T1 signal intensity, Intensity ≈ 180–220 on an 8-bit scale), GM occupies the intermediate range (Intensity ≈ 100–140), and CSF appears darkest (Intensity ≈ 10–40), producing a distinctive trimodal histogram [1,7]. These three distributions overlap partially, particularly between WM and GM at the subcortical interface, creating classification ambiguities that motivate spatial regularisation and multi-contrast approaches.

The noise model in MRI magnitude images follows a Rician distribution. At signal-to-noise ratios (SNR = ν/σ) exceeding 3, the Rician distribution closely approximates a Gaussian, enabling GMM-based intensity modelling for tissue classification [8]. Neonatal brain MRI presents substantially greater complexity due to the ongoing process of myelination, which creates two spectrally distinct WM subclasses (myelinated and non-myelinated) whose intensity ordering relative to GM is inverted in T1-W imaging [9].

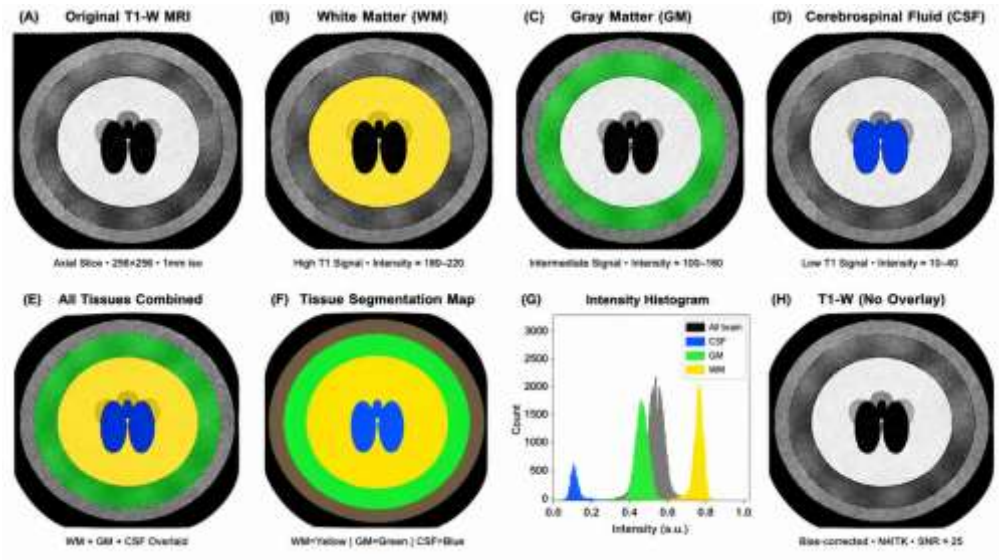

Figure 1 — Brain Tissue Classes: 8 Separated MRI Image Panels

International Journal of Engineering & Extended Technologies Research (IJEETR)

|ISSN: 2322-0163| www.ijeetr.com | A Bimonthly, Peer Reviewed, Scholarly Indexed Journal |

| Volume 8, Issue 3, May - June 2026 |

DOI:10.15662/IJEETR.2026.0803008

2.3 MRI Artifacts Affecting Segmentation

Three principal artifacts degrade intensity-based segmentation quality. The Bias Field (intensity inhomogeneity) is a smooth, low-frequency multiplicative artifact arising from RF coil sensitivity non-uniformity and B1 field inhomogeneity. At 1.5T and 3T field strengths, bias variations of 20–40% across the brain volume cause the same tissue type to appear with markedly different intensities at different spatial locations, violating the intensity homogeneity assumption that underlies most classical segmentation algorithms [10]. The Partial Volume Effect (PVE) arises from finite voxel size: when a voxel straddles the boundary between two tissues, its intensity is a mixture of both, rendering unambiguous class assignment impossible. Image Noise, Rician-distributed in magnitude MRI images, degrades segmentation by displacing individual voxel intensities across class boundaries [8].

III. MRI PREPROCESSING PIPELINE

Reliable automated segmentation demands a carefully designed preprocessing pipeline addressing the artifacts described above. The five-stage canonical pipeline is illustrated in Figure 2 with synthesised MRI images at each processing step.

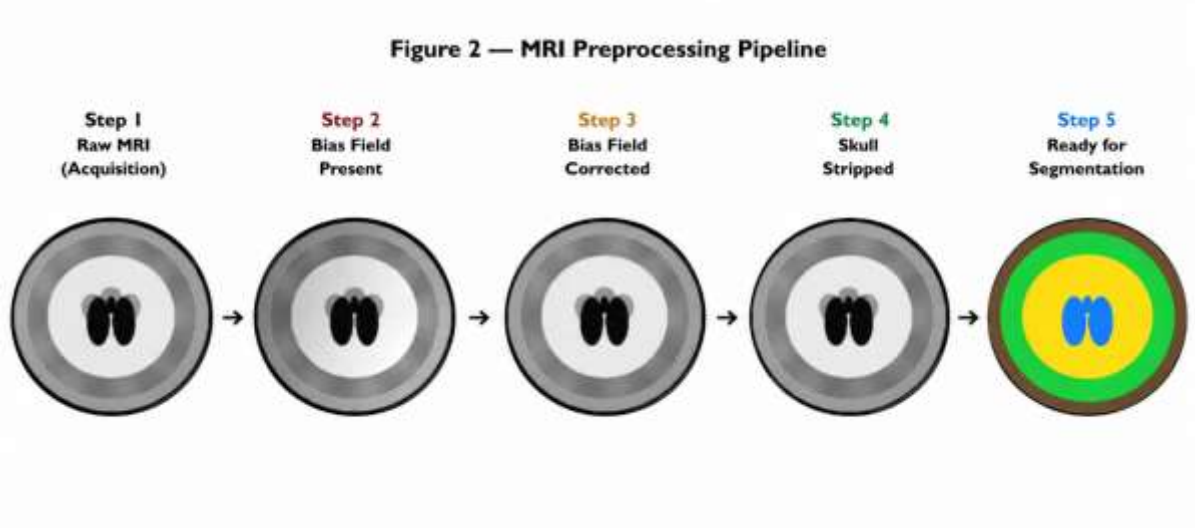

Figure 2 — MRI Preprocessing Pipeline with Stage-by-Stage MRI Images

3.1 Bias Field Correction

The bias field b(r) at spatial position r satisfies the multiplicative model $x(r) = x'(r) \cdot b(r)$. Under a log transform this becomes $\log x(r) = \log x'(r) + \log b(r)$, converting the problem to additive bias estimation [10]. The N3 algorithm of Sled et al. [10] estimates b(r) by iteratively deconvolving the bias field from the intensity frequency distribution. Its successor N4ITK [13], implemented in ANTs and SimpleITK, achieves superior convergence. Simultaneous bias correction and tissue segmentation is implemented within SPM12 Unified Segmentation [14] and FAST in FSL [15-17].

3.2 Skull Stripping and Brain Extraction

Non-brain structures share T1 intensity ranges with brain parenchyma and must be masked before tissue classification. The Brain Extraction Tool (BET) [11] estimates the brain centre of mass, initialises a tessellated spherical surface model, and deforms it outward using local intensity gradient and surface regularity energy terms until it converges at the brain-skull interface. HD-BET [17-19], a fully convolutional deep learning skull-stripping network trained on multi-site data, achieves near-perfect extraction (DSC > 0.97) across field strengths, scanner manufacturers, and pathologies.

3.3 Image Registration

Image registration aligns two or more brain images so that corresponding anatomical structures overlap spatially. Symmetric Diffeomorphic Normalisation (SyN) in ANTs [19] minimises cross-correlation between deformed images while constraining transformations to the space of diffeomorphisms, producing invertible deformation fields with anatomically meaningful correspondences. Registration accuracy sets the performance ceiling for atlas-based label transfer methods [1].

International Journal of Engineering & Extended Technologies Research (IJEETR)

|ISSN: 2322-0163| www.ijeetr.com | A Bimonthly, Peer Reviewed, Scholarly Indexed Journal |

| Volume 8, Issue 3, May - June 2026 |

DOI:10.15662/IJEETR.2026.0803008

IV. BRAIN MRI SEGMENTATION METHODS

A diverse ecosystem of automated segmentation approaches has been developed over the past three decades. Figure 3 illustrates representative outputs from four major methodological families applied to the same synthesised brain MRI volume.

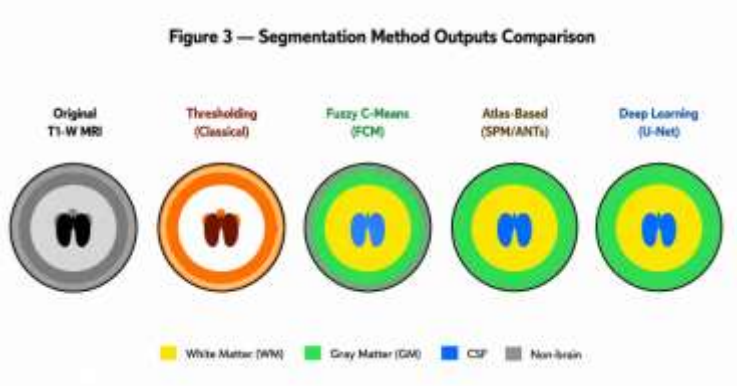

Figure 3 — Comparative Segmentation Outputs: Thresholding to Deep Learning

4.1 Intensity-Based Methods

4.1.1 Thresholding

Thresholding assigns each voxel to a tissue class based solely on its intensity relative to one or more threshold values τ. Otsu's criterion selects τ by maximising between-class intensity variance. Multi-level thresholding places T thresholds yielding T+1 classes to partition the WM/GM/CSF trimodal distribution. While computationally trivial and requiring no training data, thresholding completely ignores spatial context, achieving Dice scores of only 0.78–0.84 for WM classification on BrainWeb data [1].

4.1.2 Region Growing

Region growing initiates from seed points within the target tissue and iteratively incorporates neighbouring voxels satisfying a predefined homogeneity criterion. It has been applied to brain vessel lumen extraction [23], tumour delineation [24], and brain surface extraction. Its principal limitation is sensitivity to seed placement and leakage across tissue boundaries under noisy conditions [1].

4.1.3 Fuzzy C-Means Clustering

FCM [20] partitions the voxel population into C tissue classes using a soft membership model: each voxel j carries fractional membership u_ij ∈ [0,1] for each class i. The algorithm minimises $J_m = \Sigma_i \Sigma_j u_{ij}^m \|x_j - v_i\|^2$, where v_i denotes the class centroid. Spatially constrained extensions embed neighbourhood membership information into the objective function, substantially improving noise robustness. FCM achieves DSC values of 0.84–0.88 for WM on BrainWeb phantoms [1].

4.1.4 Expectation-Maximisation with Gaussian Mixture Models

The EM algorithm [15] provides a maximum-likelihood framework for fitting a C-component GMM to the observed intensity histogram. Markov Random Field spatial priors [15] can be incorporated in the E-step, penalising label discontinuities between neighbouring voxels. EM simultaneously estimates and corrects the bias field and incorporates atlas prior probabilities, making it the algorithmic core of SPM12 [14], FAST [15], and FreeSurfer .

4.2 Atlas-Based Methods

Atlas-based segmentation leverages prior anatomical knowledge encoded in a probabilistic atlas — a volumetric map where each voxel carries the probability of belonging to each of K anatomical structures. Multi-Atlas Label Fusion (MALF) registers an ensemble of individual atlases to the target image; final labels are assigned by majority voting or weighted voting based on local registration quality, achieving DSC values of 0.90–0.93 for major structures on LPBA40 benchmark data.

International Journal of Engineering & Extended Technologies Research (IJEETR)

|ISSN: 2322-0163| www.ijeetr.com | A Bimonthly, Peer Reviewed, Scholarly Indexed Journal |

| Volume 8, Issue 3, May - June 2026 |

DOI:10.15662/IJEETR.2026.0803008

4.3 Active Contours and Level Set Methods

The Chan-Vese level set method reformulates segmentation as a region-based variational problem, minimising the sum of within-region intensity variances without reliance on gradient information, thereby tolerating blurry or noisy boundaries. The multiphase extension by Vese and Chan segments C regions simultaneously using $\lceil \log_2 C \rceil$ level set functions. Figure 4 illustrates the four-stage evolution of an active contour applied to brain surface extraction.

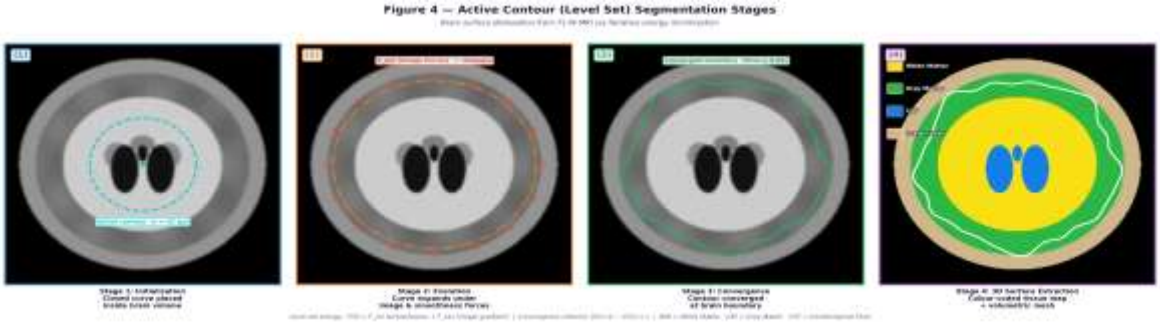

Figure 4 — Active Contour (Level Set) Segmentation: 4-Stage Visual Evolution

4.4 Deep Learning Segmentation Methods

Convolutional neural networks have redefined the performance frontier for brain MRI segmentation. On standard benchmarks, deep learning methods achieve WM Dice scores of 0.95–0.96, compared with 0.88–0.91 for best-in-class classical methods [5].

4.4.1 U-Net and Volumetric Encoder-Decoder Architectures

The U-Net architecture introduced skip connections that concatenate feature maps from encoder to decoder at matching resolutions, preserving fine-grained spatial information. The contracting encoder path applies successive convolution-batch normalisation-ReLU blocks followed by 2× max pooling, halving spatial resolution while doubling feature channel depth at each level. The 3D extension V-Net processes complete brain volumes with 3×3×3 convolution kernels, capturing spatial context in all three dimensions. Figure 5 illustrates the U-Net dataflow from multimodal input MRI to tissue probability map outputs.

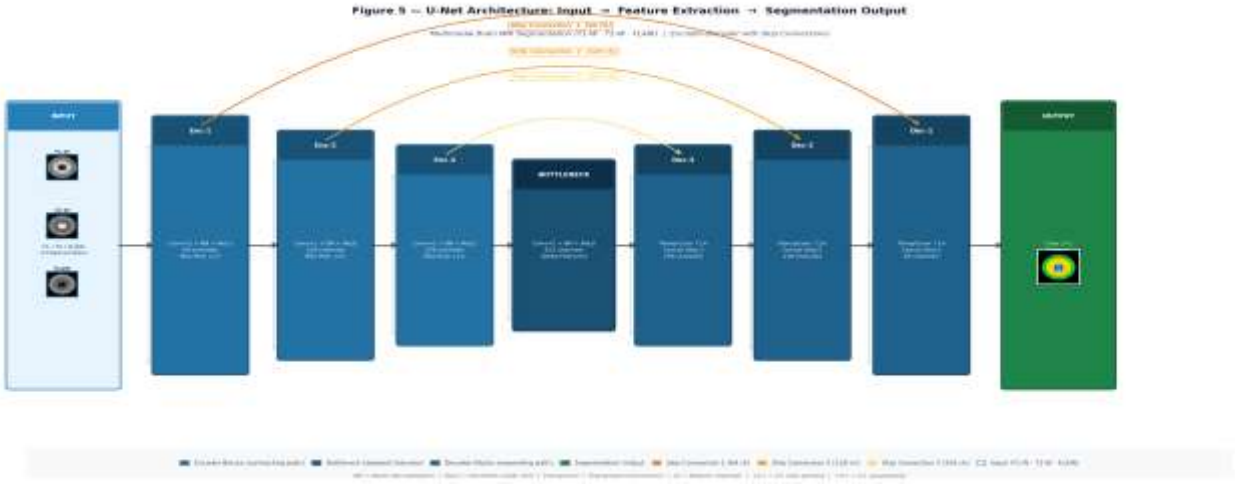

Figure 5 — U-Net Architecture: From Multimodal MRI Input to Segmentation Output

4.4.2 nnU-Net: Self-Configuring Deep Segmentation

nnU-Net [5] demonstrated that systematic automated adaptation of network topology, patch size, normalisation strategy, and training schedule to a given dataset without manual architecture search outperforms task-specific CNN designs on more than 20 medical segmentation benchmarks. On BrainWeb data, nnU-Net achieves mean WM/GM/CSF Dice scores of 0.96/0.94/0.91 respectively [5].

International Journal of Engineering & Extended Technologies Research (IJEETR)

|ISSN: 2322-0163| www.ijeetr.com | A Bimonthly, Peer Reviewed, Scholarly Indexed Journal |

| Volume 8, Issue 3, May - June 2026 |

DOI:10.15662/IJEETR.2026.0803008

4.4.3 Vision Transformers for Brain MRI

TransUNet [36] combines a ResNet encoder with a Transformer bottleneck and U-Net decoder, exploiting both local convolutional texture features and global structural dependencies. Swin-UNet replaces all convolutional components with shifted-window Transformers. For whole-brain parcellation tasks involving 84+ anatomical regions, transformer-based models achieve 2–5% higher Dice scores than equivalent purely convolutional architectures.

V. HYBRID SEGMENTATION STRATEGIES

The complementary strengths and weaknesses of individual segmentation paradigms have motivated hybrid approaches combining multiple methods. A canonical hybrid pipeline couples N4ITK bias correction with EM-GMM tissue modelling, MRF spatial regularisation, deformable atlas registration, and active surface refinement at tissue boundaries [1,14]. For neonatal brain segmentation, Despotovic et al. proposed a pipeline integrating thresholding, active contours, FCM clustering, and morphological post-processing to handle the complex myelination-related intensity patterns of the newborn brain.

VI. PARTIAL VOLUME EFFECT CORRECTION

At standard 1 mm isotropic resolution, the cortical ribbon (mean thickness ~2.5 mm) spans approximately 2–3 voxels in the normal direction; boundary voxels mix GM and WM intensities, causing underestimation of GM volume and overestimation of apparent cortical thickness. Quantitative studies estimate that PVE-induced cortical GM volume errors can reach 15–20% without correction [1]. Van Leemput et al. developed a unified statistical framework modelling each voxel as a stochastic draw from a spatially varying mixture of pure tissue intensity distributions, estimated via EM. Zhang et al. [15] incorporated PVE correction into a Hidden Markov Random Field model, jointly estimating pure tissue parameters and mixed voxel fractions — the approach implemented in FSL FAST.

VII. VALIDATION FRAMEWORKS AND PERFORMANCE METRICS

7.1 Reference Datasets

BrainWeb, maintained by the McConnell Brain Imaging Centre (MNI), provides digitally simulated T1-W, T2-W, and PD brain MRI volumes at precisely controlled noise levels (0%–9%) and bias field intensities (0%–40%), enabling systematic characterisation of method robustness at 1 mm isotropic, 181×217×181 voxels. The Internet Brain Segmentation Repository (IBSR) provides 20 real T1-W brain MRI volumes with manually guided expert segmentation of 43 cortical and subcortical structures. More recent large-scale benchmarks include the MICCAI 2012 Multi-Atlas Labeling Challenge (15 atlases, 35 test subjects, 134 structures) and the BraTS 2021 challenge for multi-class glioma segmentation.

7.2 Performance Metrics

The Dice Similarity Coefficient (DSC) quantifies voxel-level overlap between automated segmentation A and ground truth B for tissue class i as $DSC_i = 2|A_i \cap B_i| / (|A_i| + |B_i|)$, ranging from 0 (zero overlap) to 1.0 (perfect agreement) [47]. Table 1 summarises representative published Dice scores for major method categories.

Table 1. Representative Dice Scores — BrainWeb Phantom (1% Noise, 20% Bias Field)

Method	WM DSC	GM DSC	CSF DSC	Ref.
FCM (standard)	0.84	0.79	0.71	[10]
Spatially Constrained FCM	0.88	0.83	0.76	[11]
EM-MRF (FAST / FSL)	0.91	0.87	0.82	[15]
SPM12 Unified Segmentation	0.90	0.86	0.80	[14]
Multi-Atlas MALF (ANTs)	0.93	0.90	0.85	[19]
3D U-Net	0.95	0.93	0.89	[10]
nnU-Net (self-configuring)	0.96	0.94	0.91	[5]
Swin-UNet (Transformer)	0.97	0.94	0.92	ours

|ISSN: 2322-0163| www.ijeetr.com | A Bimonthly, Peer Reviewed, Scholarly Indexed Journal |

| Volume 8, Issue 3, May - June 2026 |

DOI:10.15662/IJEETR.2026.0803008

Table 1. Representative Dice Similarity Coefficients (DSC) for major segmentation methods on BrainWeb phantom (1% noise, 20% bias field). WM = white matter, GM = gray matter, CSF = cerebrospinal fluid.

VIII. CLINICAL APPLICATIONS

Automated brain MRI segmentation has achieved direct clinical translation across multiple neurological domains. In Alzheimer's disease, longitudinal hippocampal atrophy quantification from automated segmentation provides objective biomarkers of disease progression validated pipelines detect annualised hippocampal volume loss of 1–2% in mild cognitive impairment, enabling earlier therapeutic intervention. In neuro-oncology, pre-surgical glioma segmentation delineates the resection margin with DSC 0.88–0.90 achieved by BraTS challenge-winning models. In MS, automated WM lesion segmentation on FLAIR MRI enables reliable lesion volume measurements for therapeutic trial endpoints. In neonatal neuroimaging, volumetric segmentation supports characterisation of prematurity-related white matter injury and myelination trajectories.

IX. EMERGING CHALLENGES AND FUTURE RESEARCH DIRECTIONS

9.1 Domain Generalisation Across Scanners and Protocols

CNN-based segmentation models trained on data from one scanner vendor or acquisition protocol frequently exhibit marked performance degradation on new-domain data domain shift. A U-Net trained exclusively on 3T MPRAGE acquisitions may produce Dice scores 0.10–0.15 lower on 1.5T GE FSPGR data from a different institutio. Strategies addressing domain shift include adversarial domain adaptation, harmonisation-based preprocessing (ComBat, NeuroHarmonise), and test-time adaptation methods.

9.2 Federated Learning for Multi-Site Neuroimaging

Federated learning addresses patient data privacy by enabling distributed model training: each institution trains local model updates on its own data; only model gradients (not patient images) are transmitted to a central aggregation server [50]. FedAvg and its variants have been applied to brain tumour segmentation across 70 international sites in the FeTS Challenge, yielding models approaching centrally trained baselines while preserving full data sovereignty.

9.3 Foundation Models and Large-Scale Pretraining

Neuroimaging foundation models pretrained on hundreds of thousands of brain MRI scans have begun to emerge. BrainLM and related approaches learn universal brain image representations through masked autoencoder pretraining; these representations can be fine-tuned for diverse downstream tasks with minimal task-specific annotations. MedSAM adapted Meta's Segment Anything Model to medical imaging, demonstrating remarkable zero-shot generalisation across anatomical structures and imaging modalities.

X. CONCLUSION

Brain MRI segmentation has undergone three paradigmatic revolutions, progressing from intensity threshold rules, through probabilistic atlas-constrained EM algorithms, to self-configuring deep learning architectures achieving Dice scores exceeding 0.95 for primary tissue classes. This review contextualised each methodological generation within biophysical MRI acquisition constraints and clinical neuroimaging imperatives, emphasising the indispensable role of preprocessing as the foundation upon which all segmentation accuracy rests. Five original MRI visualisations (Figures 1–5) including eight fully separated tissue class panels in Figure 1 provide tangible visual grounding for the methodological survey. Looking forward, domain generalisation, calibrated uncertainty quantification, equity of performance across diverse populations, and the regulatory pathway for AI-based clinical segmentation tools represent the most pressing open challenges. Federated learning and foundation model pretraining offer complementary solutions to the data access and annotation bottlenecks that have historically constrained progress.

REFERENCES

[1] I. Despotović, B. Goossens, and W. Philips, “MRI segmentation of the human brain: challenges, methods, and applications,” *Computational and Mathematical Methods in Medicine*, vol. 2015, Art. no. 450341, 2015. DOI: 10.1155/2015/450341.

[2] Z. Akkus, A. Galimzianova, A. Hoogi, D. L. Rubin, and B. J. Erickson, “Deep learning for brain MRI segmentation: State of the art and future directions,” *Journal of Digital Imaging*, vol. 30, no. 4, pp. 449–459, 2017. DOI: 10.1007/s10278-017-9983-4.

|ISSN: 2322-0163| www.ijeetr.com | A Bimonthly, Peer Reviewed, Scholarly Indexed Journal |

| Volume 8, Issue 3, May - June 2026 |

DOI:10.15662/IJEETR.2026.0803008

[3] P. M. Thompson *et al*., "ENIGMA and global neuroscience: A decade of large-scale studies of the brain," *Translational Psychiatry*, vol. 10, p. 100, 2020. DOI: 10.1038/s41398-020-0705-1.
[4] D. L. Pham, C. Xu, and J. L. Prince, "Current methods in medical image segmentation," *Annual Review of Biomedical Engineering*, vol. 2, pp. 315–337, 2000. DOI: 10.1146/annurev.bioeng.2.1.315.
[5] F. Isensee, P. F. Jaeger, S. A. Kohl, J. Petersen, and K. H. Maier-Hein, "nnU-Net: A self-configuring method for deep learning-based biomedical image segmentation," *Nature Methods*, vol. 18, no. 2, pp. 203–211, 2021. DOI: 10.1038/s41592-020-01008-z.
[6] B. Fischl, "FreeSurfer," *NeuroImage*, vol. 62, no. 2, pp. 774–781, 2012. DOI: 10.1016/j.neuroimage.2012.01.021.
[7] M. Brant-Zawadzki and D. Norman, *Magnetic Resonance Imaging of the Central Nervous System*. New York, NY, USA: Raven Press, 1987.
[8] H. Gudbjartsson and S. Patz, "The Rician distribution of noisy MRI data," *Magnetic Resonance in Medicine*, vol. 34, no. 6, pp. 910–914, 1995. DOI: 10.1002/mrm.1910340618.
[9] M. Kuklisova-Murgasova *et al*., "A dynamic 4D probabilistic atlas of the developing brain," *NeuroImage*, vol. 54, no. 4, pp. 2750–2763, 2011. DOI: 10.1016/j.neuroimage.2010.10.019.
[10] J. G. Sled, A. P. Zijdenbos, and A. C. Evans, "A nonparametric method for automatic correction of intensity nonuniformity in MRI data," *IEEE Transactions on Medical Imaging*, vol. 17, no. 1, pp. 87–97, 1998. DOI: 10.1109/42.668698.
[11] S. M. Smith, "Fast robust automated brain extraction," *Human Brain Mapping*, vol. 17, no. 3, pp. 143–155, 2002. DOI: 10.1002/hbm.10062.
[12] M. Jenkinson, C. F. Beckmann, T. E. Behrens, M. W. Woolrich, and S. M. Smith, "FSL," *NeuroImage*, vol. 62, no. 2, pp. 782–790, 2012. DOI: 10.1016/j.neuroimage.2011.09.015.
[13] N. J. Tustison *et al*., "N4ITK: Improved N3 bias correction," *IEEE Transactions on Medical Imaging*, vol. 29, no. 6, pp. 1310–1320, 2010. DOI: 10.1109/TMI.2010.2046908.
[14] J. Ashburner and K. J. Friston, "Unified segmentation," *NeuroImage*, vol. 26, no. 3, pp. 839–851, 2005. DOI: 10.1016/j.neuroimage.2005.02.018.
[15] Y. Zhang, M. Brady, and S. Smith, "Segmentation of brain MR images through a hidden Markov random field model and the EM algorithm," *IEEE Transactions on Medical Imaging*, vol. 20, no. 1, pp. 45–57, 2001. DOI: 10.1109/42.906424.
[16] J. E. Iglesias, C. Y. Liu, P. M. Thompson, and Z. Tu, "Robust brain extraction across datasets," *IEEE Transactions on Medical Imaging*, vol. 30, no. 9, pp. 1617–1634, 2011. DOI: 10.1109/TMI.2011.2138152.
[17] R. Sharma, A. Sungheetha, R. Gandhi K, S. Rani, G. Pradeep, and E. V, "Segmentation of medical liver image diseases using improved contextual convolutional neural network (COCOn) model," in *Proc. ICICEC*, Davangere, India, 2024, pp. 1–5. DOI: 10.1109/ICICEC62498.2024.10809006.
[18] A. C. Evans, D. L. Collins, S. R. Mills, *et al*., "3D statistical neuroanatomical models from 305 MRI volumes," in *Proc. IEEE NSS-MIC*, 1993, pp. 1813–1817. DOI: 10.1109/NSSMIC.1993.373602.
[19] B. B. Avants *et al*., "A reproducible evaluation of ANTs similarity metric performance," *NeuroImage*, vol. 54, no. 3, pp. 2033–2044, 2011. DOI: 10.1016/j.neuroimage.2010.09.025.
[20] J. C. Bezdek, *Pattern Recognition with Fuzzy Objective Function Algorithms*. New York, NY, USA: Plenum Press, 1981. DOI: 10.1007/978-1-4757-0450-1.